

# Mechanism of Gold-Assisted Exfoliation of Centimeter-Sized Transition Metal Dichalcogenide Monolayers

*Matěj Velický, \*<sup>1,2,3</sup> Gavin E. Donnelly,<sup>1</sup> William R. Hendren,<sup>1</sup> Stephen McFarland,<sup>1</sup> Declan Scullion,<sup>1</sup> William J. I. DeBenedetti,<sup>3</sup> Gabriela Calinao Correa,<sup>4</sup> Yimo Han,<sup>5</sup> Andrew J. Wain,<sup>6</sup> Melissa A. Hines,<sup>3</sup> David A. Muller,<sup>5,7</sup> Kostya S. Novoselov,<sup>2</sup> Héctor D. Abruña,<sup>3</sup> Robert M. Bowman,<sup>1</sup> Elton J. G. Santos,<sup>1</sup> and Fumin Huang\*<sup>1</sup>*

<sup>1</sup> School of Mathematics and Physics, Queen's University Belfast, University Road, Belfast, BT7 1NN, UK

<sup>2</sup> School of Physics and Astronomy, University of Manchester, Oxford Road, Manchester, M13 9PL, UK

<sup>3</sup> Department of Chemistry and Chemical Biology, Cornell University, Ithaca, NY, 14853, USA

<sup>4</sup> Department of Material Science and Engineering, Cornell University, Ithaca, NY, 14853, USA

<sup>5</sup> School of Applied and Engineering Physics, Cornell University, Ithaca, NY, 14853, USA

<sup>6</sup> National Physical Laboratory, Teddington, TW11 0LW, UK

<sup>7</sup> Kavli Institute at Cornell for Nanoscale Science, Ithaca, NY, 14853, USA

**KEYWORDS:** TMDC, MoS<sub>2</sub>, gold, monolayer exfoliation, surface modification

## ABSTRACT

Exfoliation of large-area monolayers is important for fundamental research and technological implementation of transition metal dichalcogenides. Various techniques have been explored to increase the exfoliation yield, but little is known about the underlying mechanism at the atomic level. Here, we demonstrate gold-assisted mechanical exfoliation of monolayer molybdenum disulfide, up to a centimeter scale. Detailed spectroscopic, microscopic, and first-principles density functional theory analyses reveal that strong van der Waals (vdW) interaction between Au and the topmost MoS<sub>2</sub> layer facilitates the exfoliation of monolayers. However, the large-area exfoliation promoted by such strong vdW interaction is only achievable on freshly-prepared clean and smooth Au surfaces, while rough surfaces and surfaces exposed to air for more than 15 min result in negligible exfoliation yields. This technique is successfully extended to MoSe<sub>2</sub>, WS<sub>2</sub>, WSe<sub>2</sub>, MoTe<sub>2</sub>, WTe<sub>2</sub> and GaSe. In addition, electrochemical characterization reveals intriguing interactions between monolayer MoS<sub>2</sub> and Au. A sub-nanometer MoS<sub>2</sub> monolayer strongly passivates the chemical properties of the underlying Au and the Au significantly modulates the electronic band structure of the MoS<sub>2</sub>, turning it from semiconducting to metallic. This could find applications in many areas, including electrochemistry, photovoltaics and photocatalysis.

Monolayer transition metal dichalcogenides (TMDCs) possess a wide range of extraordinary optoelectronic, chemical and mechanical properties unattainable in their bulk form.<sup>1-3</sup>

Many bulk TMDCs are semiconductors with an indirect band-gap, which transitions to a direct band-gap when in monolayer form, rendering them excellent materials for optoelectronics.<sup>4-6</sup> A major challenge for large-scale application of TMDCs is the competition between material quality and production scalability. For instance, readily scalable liquid-phase exfoliation is tainted by the small size, poor quality, and contamination of the resulting crystals.<sup>7</sup> Chemical vapor deposition yields large-area monolayers but their quality is inferior to those made by mechanical exfoliation (ME), and the method is time-consuming and costly.<sup>8</sup> By contrast, ME generally yields the highest quality monolayer TMDCs, however, their typical lateral dimensions are in the range of tens to hundreds of microns.<sup>9-10</sup> This poses a significant challenge since many characterization techniques, large-scale processing, and applications typically require macroscopic samples. Finding a facile way of producing large, high-quality monolayer TMDCs is therefore crucial for both fundamental research and technology advancement.

Various techniques have been explored to improve the exfoliation yield. Gold is known to have a strong affinity for sulfur, which has been exploited to enhance the exfoliation of monolayer molybdenum disulfide.<sup>11-12</sup> However, little detail about the underlying mechanism was provided and the largest MoS<sub>2</sub> size was limited to a few hundreds of microns. A comprehensive understanding of the gold-assisted large-area exfoliation at the atomic level is therefore necessary for devising techniques for the mass production of macroscopic TMDC monolayers, whose small lateral size has previously limited research and technological developments.

Here, we present a facile gold-assisted mechanical exfoliation of extraordinarily large monolayer MoS<sub>2</sub>, up to a centimeter size (Figure 1), and provide detailed investigation on the exfoliation mechanism. Raman spectroscopy, photoluminescence (PL) measurements, X-ray

photoelectron spectroscopy (XPS) and scanning transmission electron microscopy (STEM) collectively reveal that the high-yield exfoliation is facilitated by van der Waals (vdW) interaction between the Au surface and the topmost MoS<sub>2</sub> layer. This interaction is stronger than the interlayer vdW interactions in bulk MoS<sub>2</sub>, therefore facilitating the exfoliation of large-area monolayer films. The cleanliness and smoothness of the Au surface are critical for the near-unity yield of monolayer MoS<sub>2</sub>, which can only be achieved on freshly-deposited Au films exposed to air for less than 6 min. The short air exposure prevents the accumulation of airborne organic contaminants on the Au surface, which otherwise weakens the vdW forces between MoS<sub>2</sub> and Au and suppresses the exfoliation. The exfoliation yield also decreases significantly with increasing surface roughness of Au. These findings are confirmed by calculations from the first-principles density functional theory (DFT). The calculated vdW binding energies of several MoS<sub>2</sub>/Au heterostructures, with varied Au–Mo separations and surface roughness, show excellent agreement with the experiments. We successfully applied this exfoliation technique to a variety of metal chalcogenides, including MoSe<sub>2</sub>, WS<sub>2</sub>, WSe<sub>2</sub>, MoTe<sub>2</sub>, WTe<sub>2</sub> and GaSe (Supporting Fig. S1), and found, that the monolayer yield is generally near-unity, limited only by the size of the parent bulk crystal.

We further discovered intriguing interactions between monolayer MoS<sub>2</sub> and the underlying Au. Electrochemical characterization, using voltammetry and scanning electrochemical microscopy (SECM), reveals that the surface density of electronic states (DOS) of MoS<sub>2</sub> is strongly modulated by the underlying Au, and conversely, that the Au substrate is endowed with the chemical properties of MoS<sub>2</sub>. This is manifested in strong passivation of the Au surface by the physisorbed monolayer MoS<sub>2</sub> for inner-sphere electron transfer, while the outer-sphere electron transfer is almost unaffected due to long-range electron tunneling. These intriguing properties bring opportunities for many applications in areas such as electrode modification and energy storage/conversion.

## RESULTS

### Exfoliation and characterization of MoS<sub>2</sub> on Au

Fig. 1a shows a macroscopic optical image of MoS<sub>2</sub> exfoliated on a 7.5 nm thick Au (111) grown by physical vapor deposition (PVD) on an SiO<sub>2</sub>/Si wafer with a 1 nm Ti adhesion layer. MoS<sub>2</sub> monolayers reach lateral dimensions beyond 1 cm, limited only by the size and quality of the parent bulk crystal. The microscopic optical image in Fig. 1b reveals good crystal uniformity with occasional breaks likely caused by lattice defects, surface contamination, and mechanical stress during exfoliation. The number of MoS<sub>2</sub> layers was unambiguously determined using optical microscopy, Raman spectroscopy, and atomic force microscopy (AFM). The high optical contrast of monolayer MoS<sub>2</sub> allows direct counting of the layers (Fig. 1c). The Raman spectra in Fig. 1d show the two main vibrational modes,  $E_{2g}^1$  (in-plane) and  $A_{1g}$  (out-of-plane), whose intensities increase monotonically with increasing number of MoS<sub>2</sub> layers ( $\leq 4L$ ), as expected.<sup>13</sup> The frequency of both modes blueshifts with the increasing MoS<sub>2</sub> thickness, which is attributed to a stiffening of the vibrations upon layer addition. An anomalous redshift of the  $E_{2g}^1$  mode, due to stacking-induced changes in intralayer bonding, is often observed on insulating substrates.<sup>10, 13-14</sup> Here we observe a blueshift of the  $E_{2g}^1$  mode, suggesting a strong interaction between MoS<sub>2</sub> and Au, which leads to an efficient charge transfer and screening of the long-range Coulomb interactions between MoS<sub>2</sub> layers. This is also consistent with the large frequency shifts of 8–10 cm<sup>-1</sup> between the 1L and 4L MoS<sub>2</sub>. AFM topography imaging across a monolayer-bilayer boundary gives a step-height of 9.8 Å (insets in Fig. 1e), which is slightly higher than theoretical thickness of 6.15 Å,<sup>3</sup> but in agreement with the literature.<sup>13, 15</sup> No PL was observed in monolayer MoS<sub>2</sub> on Au (Supporting Fig. S2) since it is completely quenched due the conformal contact between MoS<sub>2</sub> and Au, consistent with previous reports.<sup>16</sup> The occasional observation of PL in

monolayer MoS<sub>2</sub> on Au,<sup>17-18</sup> could be caused by an increased physical separation due to polymer residues and airborne contaminants at the MoS<sub>2</sub>/Au interface.

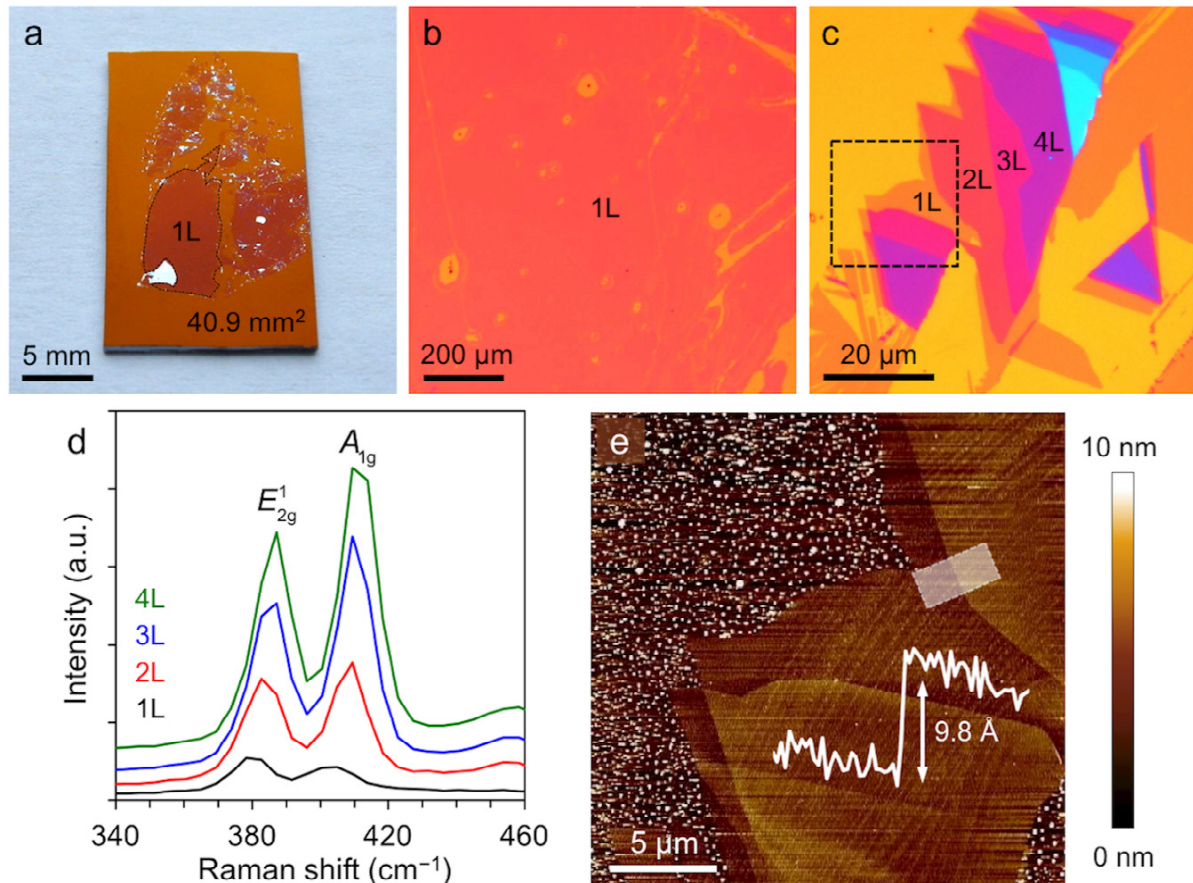


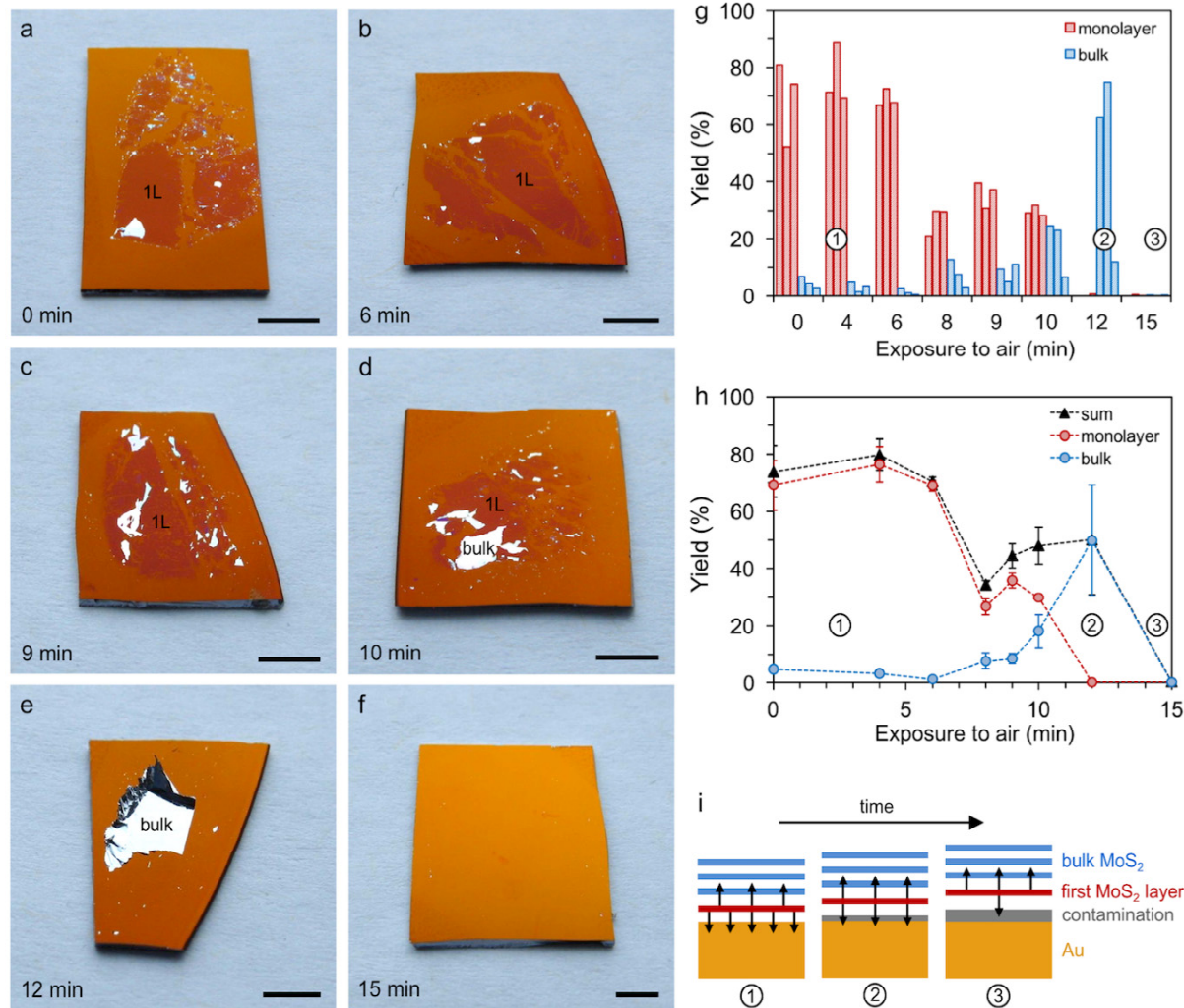
**Figure 1 | Exfoliation and characterization of MoS<sub>2</sub> on Au substrate.** **a**, Optical macrograph of a large-area monolayer MoS<sub>2</sub> on a 7.5 nm Au/1 nm Ti/93 nm SiO<sub>2</sub>/Si wafer. **b**, Optical micrograph of a large-area monolayer MoS<sub>2</sub>. **c**, High-resolution optical micrographs of the mono- and multi-layer MoS<sub>2</sub>. **d**, Raman spectra (532 nm excitation) of mono- and multi-layer MoS<sub>2</sub> in **c**, showing the main in-plane ( $E_{2g}^1$ ) and out-of-plane ( $A_{1g}$ ) vibrational modes (spectra are offset for clarity). **e**, AFM topography image taken from the area highlighted in **c** by the black square, showing a smooth MoS<sub>2</sub> surface and tape residue on the Au surface. Inset: corresponding height profiles of monolayer-bilayer boundary, taken from the area highlighted by the white rectangle.

## Mechanism of the large-area exfoliation

We found that the exfoliation critically depends on the surface condition of Au, governed specifically by the Au roughness and the ageing of the Au surface since its deposition under ultra-high vacuum. The average areal yield of exfoliation, expressed as the percentage of Au surface covered with MoS<sub>2</sub> (see Methods), is large (70–80%, predominantly monolayer) on freshly-prepared Au, but gradually decreases with the time of Au exposed to air, with an increasingly larger proportion of bulk MoS<sub>2</sub> (Figure 2). After 15 min, almost no crystals are exfoliated (yield < 0.5%). This suggests that the adhesion forces between MoS<sub>2</sub> and Au strongly depend on how long the Au surface has aged in air, which we summarize in the following three stages (Fig. 2g–i): Initially (1), the adhesion between Au and the first MoS<sub>2</sub> layer is stronger than the interaction between the first MoS<sub>2</sub> layer and the rest of MoS<sub>2</sub>, resulting in the predominant exfoliation of monolayer MoS<sub>2</sub>. Gradually (2), the MoS<sub>2</sub>–Au adhesion weakens and becomes comparable to the interlayer interactions in bulk MoS<sub>2</sub>, facilitating more efficient exfoliation of thicker MoS<sub>2</sub> (governed by lattice defects), giving rise to a peak in the bulk yield (Fig. 2g–h). In the end (3), the MoS<sub>2</sub>–Au adhesion becomes weaker than the interlayer interaction in bulk MoS<sub>2</sub> and the exfoliation is negligible.

The above phenomenon is caused by the adsorption of organic airborne contaminants, which transform the freshly deposited Au surface from hydrophilic to hydrophobic. This was shown by Smith, who confirmed that while a clean Au surface is hydrophilic, exposure to air (but also prolonged dwell time under vacuum) leads to a sub-monolayer of carbonaceous contamination, which quickly turns the Au surface hydrophobic.<sup>19</sup> This was manifested by an abrupt increase of water contact angle (WCA) on Au by about 30°–40° within 10 min. Indeed, we found that the WCA on Au exposed to air rapidly increases by 15°–30° in the first 15 min (Supporting Fig. S3), following the same trend as the exfoliation yield (Fig. 2). The contamination

layer increases the separation between  $\text{MoS}_2$  and Au, weakens the adhesion forces between the two, and consequently reduces the exfoliation yield.



We further found that the yield of monolayer MoS<sub>2</sub> notably decreases with increasing thickness of the Au films, as shown in Fig. 3a–c for 7.5 nm and 100 nm thick Au. The scanning electron microscopy (SEM) images in Fig. 3d–e show that the surface of the 7.5 nm Au is smoother than that of the 100 nm Au, which is further quantified by the AFM topography images in Fig. 3f–g. The higher surface roughness of the thicker Au film therefore appears to weaken the vdW interactions between Au and MoS<sub>2</sub>, due to increased physical separation at surface depressions, also supported by theoretical calculations below. The best exfoliation results are achieved on thin Au films of 5–20 nm with root mean square (RMS) roughness < 1 nm. Despite the polycrystalline nature of the Au films evident from SEM and AFM, the predominant crystal orientation was found to be Au (111) by X-ray diffraction (XRD) measurements (Supporting Fig. S4). This is typical for Au PVD films grown on various substrates, using different deposition conditions,<sup>20-22</sup> and expected from the lowest energy of the Au (111) surface.<sup>23</sup>

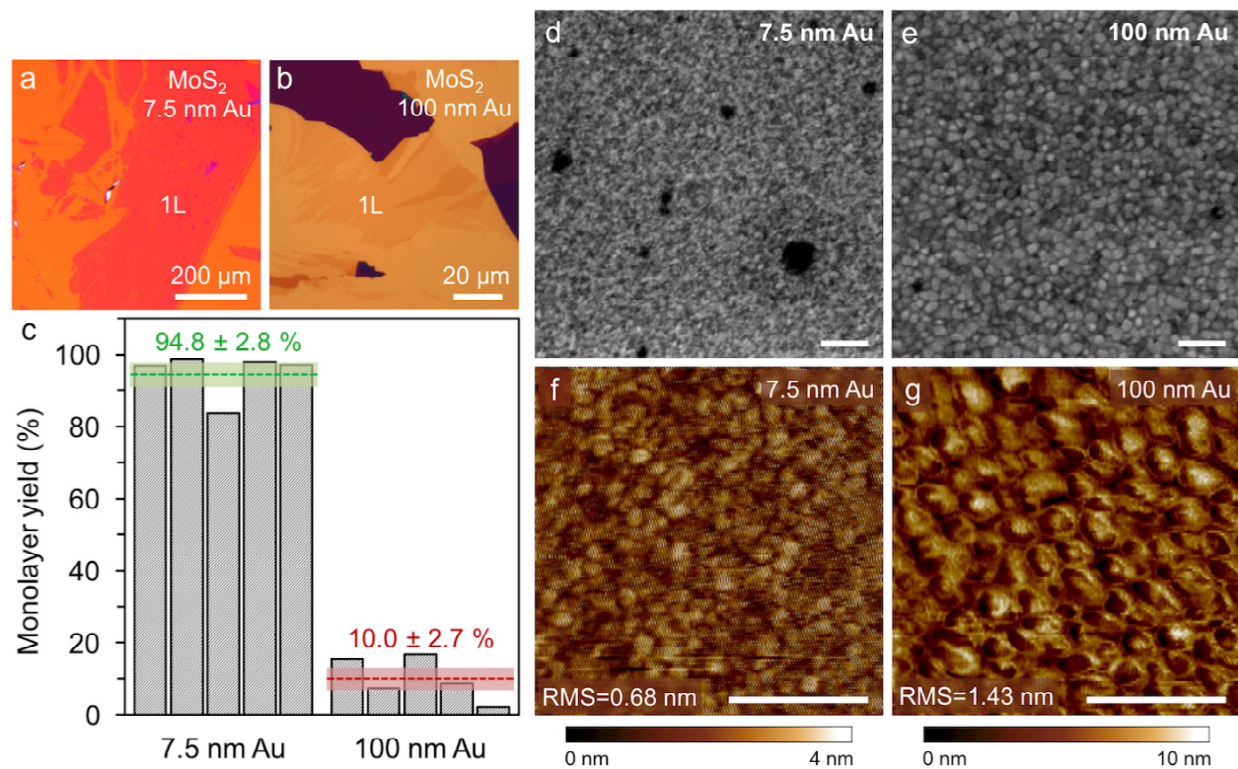


**Figure 3 | Dependence of monolayer MoS<sub>2</sub> exfoliation yield on Au roughness.** **a–b**, Optical micrographs of MoS<sub>2</sub> exfoliated on 7.5 nm and 100 nm Au, respectively. **c**, Quantification of the monolayer yield for 7.5 nm and 100 nm Au. A constant area of 12,100  $\mu\text{m}^2$  (110  $\times$  110  $\mu\text{m}^2$ ) was used in all quantifications. **d–e**, SEM images of 7.5 nm and 100 nm Au substrates, showing continuous polycrystalline Au coverage with occasional voids and grain sizes varying from 10–20 nm to 40–60 nm for 7.5 nm to 100 nm thick Au, respectively. **f–g**, AFM images of the same substrates taken immediately after Au deposition, showing indentations within the grains of 100 nm Au and the RMS roughness of the surface. Scale bars in **d–g** correspond to 200 nm.

## The nature of MoS<sub>2</sub>–Au interaction

The MoS<sub>2</sub> interaction with Au was predicted to be of vdW nature due to weak hybridization.<sup>24–25</sup> However, few have provided direct experimental evidence of Au-MoS<sub>2</sub> interaction. Here we employed STEM to image the separation between monolayer MoS<sub>2</sub> and Au. The left-hand side of the high-angle annular dark-field (HAADF)-STEM image in Fig. 4a shows a region of a clean monolayer MoS<sub>2</sub>/Au interface. The average closest separation between the center of the Mo and Au planes is  $5.1 \pm 0.3$  Å, close to the value of 4.5 Å obtained from theoretical calculations below. This implies a 3.5 Å spacing between the Au and S planes,  $\sim 17\%$  larger than the interlayer vdW spacing in bulk MoS<sub>2</sub> (3.0 Å)<sup>3</sup> and  $\sim 59\%$  larger than a covalent Au–S bond (2.2 Å),<sup>26</sup> confirming that the MoS<sub>2</sub>–Au interaction is strong vdW rather than covalent in nature. Monolayer MoS<sub>2</sub> maintains the spacing due to its conformity with the underlying Au, as seen from the step in the top-right area of Fig. 4a. A schematic model of the MoS<sub>2</sub>/Au heterostructure is shown in Fig. 4b.

We also employed XPS to further investigate the interaction between MoS<sub>2</sub> and Au. The high-resolution spectra of the Mo 3d and S 2p regions in Fig. 4c–d reveal that the binding energies in monolayer MoS<sub>2</sub> decrease by  $\sim 0.4$  eV in comparison to bulk MoS<sub>2</sub>. This suggests that there is a significant degree of charge transfer between monolayer MoS<sub>2</sub> and Au, consistent with the observed PL quenching. Almost identical shifts (0.4–0.5 eV) were observed in other MoS<sub>2</sub>–Au systems, and explained by the formation of a Schottky barrier at the MoS<sub>2</sub>/Au interface<sup>27</sup> and charge transfer from Au to MoS<sub>2</sub>, leading to an increase of the electron density at the interface.<sup>28–29</sup> Crucially, the lack of changes in the shape and width of the XPS peaks in our work confirms that monolayer MoS<sub>2</sub> maintains its chemical identity upon exfoliation (detailed XPS spectra including the peak fittings are shown in Supporting Fig. S5).

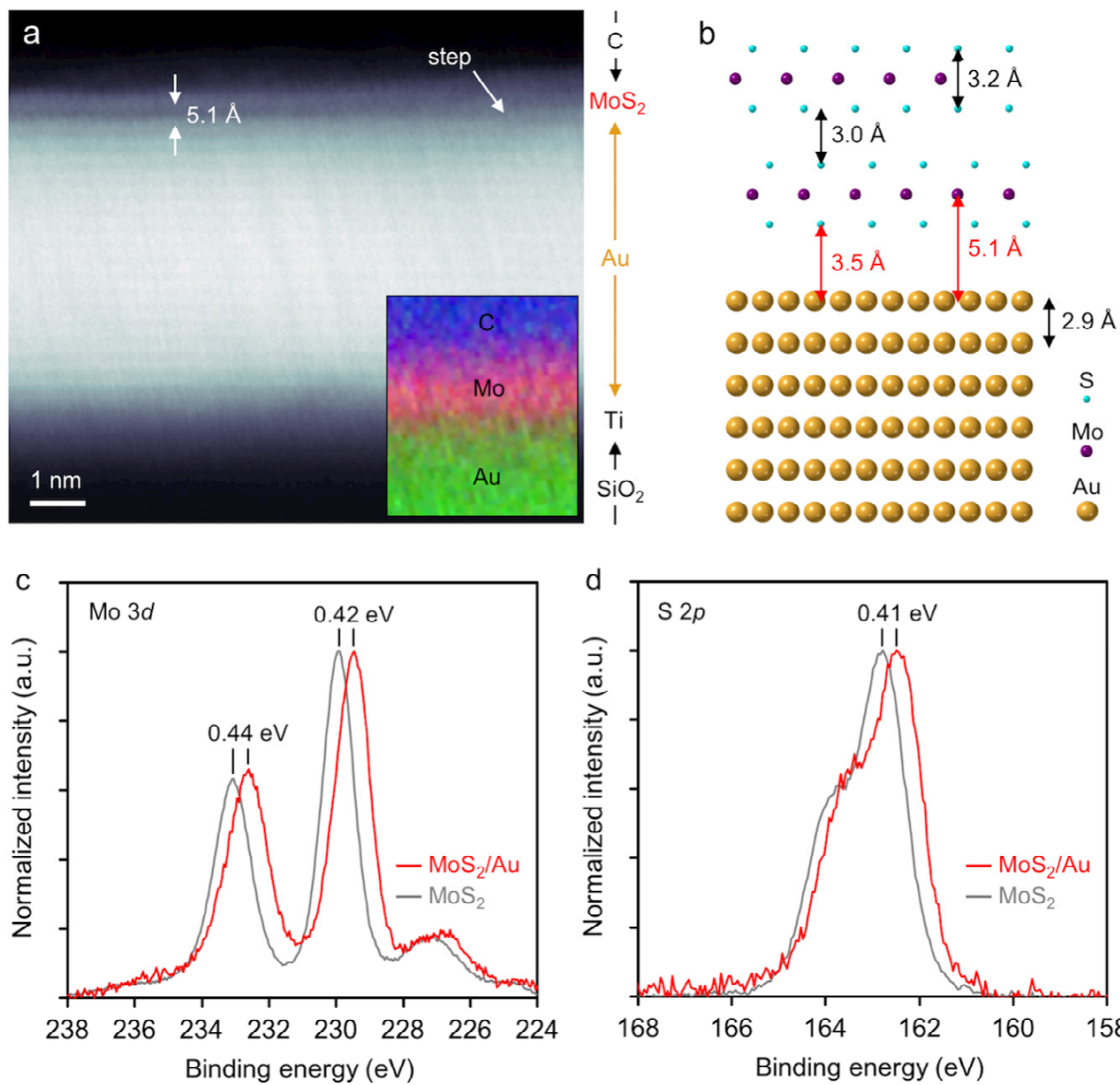


**Figure 4 | STEM and XPS characterization of monolayer MoS<sub>2</sub> on Au.** **a**, HAADF-STEM image of monolayer MoS<sub>2</sub> on 5 nm Au showing a region of clean MoS<sub>2</sub>/Au interface with an average Mo-Au separation of 5.1 Å. Inset: Electron energy loss spectroscopy (EELS) composite image acquired from the middle region of the image, confirming the presence of Au, Mo, and C. **b**, A schematic structure model of the MoS<sub>2</sub>/Au heterostructure. The distances in red are determined from HAADF-STEM, the distances in black are the lattice parameters of bulk MoS<sub>2</sub> and Au.<sup>3, 30</sup> **c-d**, High-resolution XPS of Mo 3d and S 2p regions of monolayer MoS<sub>2</sub>/Au (red) and bulk MoS<sub>2</sub> (gray), showing a shift in the binding energy due to charge transfer. The binding energies were obtained from Gaussian fits of the baseline-subtracted Mo 3d and S 2p spectra.

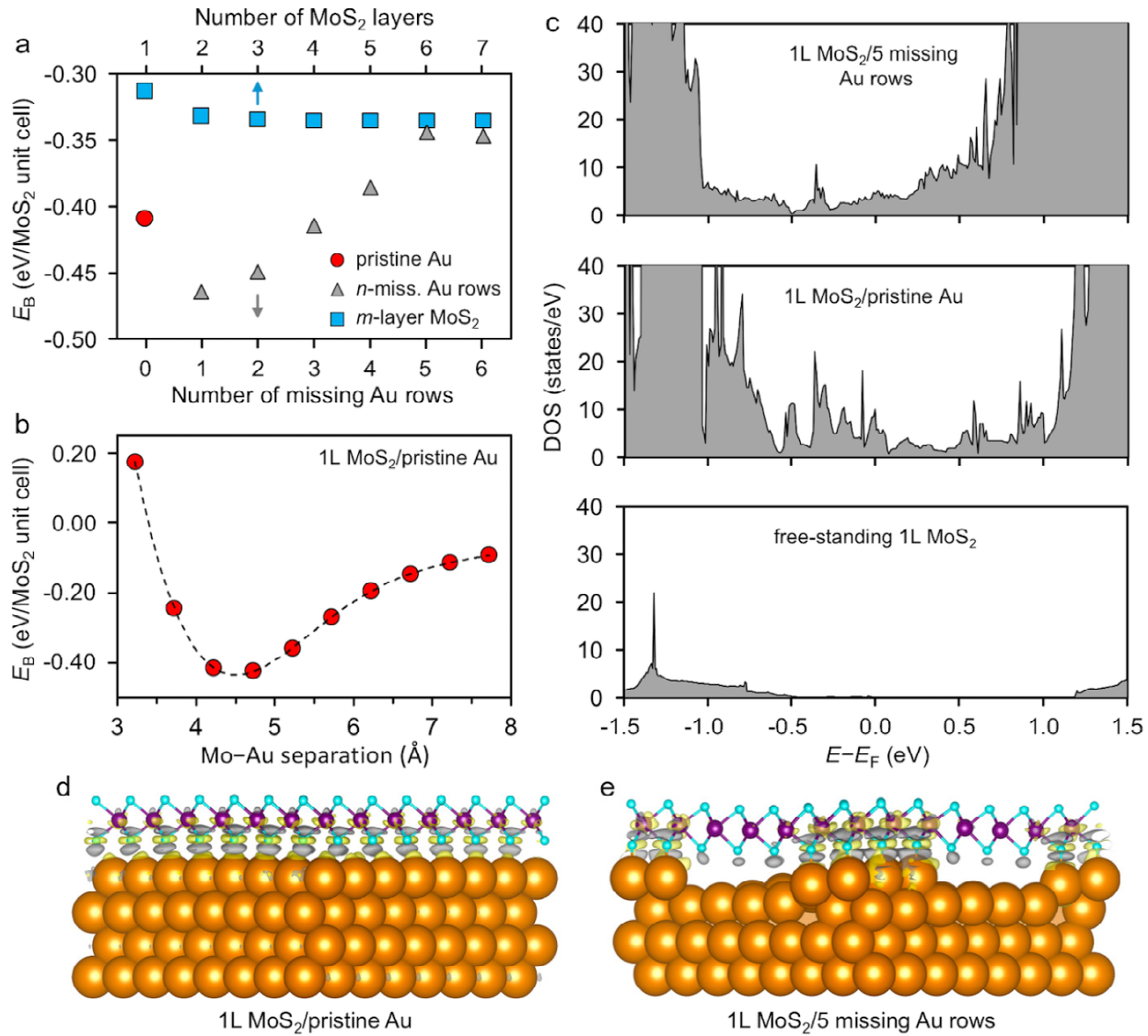
To further elucidate the interaction between monolayer MoS<sub>2</sub> and Au, we performed first-principles atomistic calculations, including vdW binding energies, for a range of different systems.

Fig. 5a shows the binding energy ( $E_B$ , per  $\text{MoS}_2$  unit cell) for monolayer  $\text{MoS}_2$  on different systems: pristine Au (111) surface, Au surface with  $n$  missing Au rows, and on  $m$ -layer  $\text{MoS}_2$ . The calculations suggest  $E_B = -0.41$  eV for monolayer  $\text{MoS}_2$  on pristine Au (Fig. 5a), which is stronger than the binding between monolayer  $\text{MoS}_2$  and bulk  $\text{MoS}_2$  ( $E_B = -0.34$  eV for  $m \geq 5$ ), supporting the predominant exfoliation of monolayers, in agreement with our earlier interpretation and other theoretical calculations.<sup>25,31</sup> The binding energy between Au and  $\text{MoS}_2$  rapidly decreases with increasing Au– $\text{MoS}_2$  separation (Fig. 5b), explaining why a sub-monolayer contamination significantly inhibits the exfoliation.

Introduction of a small number of surface Au vacancies or adatoms is found to have negligible effects on the binding energy (−0.42 eV). Conversely, when a large vacancy in the form of  $n$  missing surface rows is introduced to the Au surface, the binding energy changes significantly. As shown in Fig. 5a, the  $E_B$  is initially high for  $n = 1$  but decreases to reach a similar magnitude to that of pristine Au for  $n = 3$ . The increased number of active sites with large amount of dangling bonds and charge density at the Au surface initially leads to stronger Au–S interaction, as seen for  $n \leq 3$ . For  $n > 3$ , the comparably poorer conformity of  $\text{MoS}_2$  to Au weakens this interaction, which becomes comparable to that of bulk  $\text{MoS}_2$  for  $n = 5$  and 6. These calculations are consistent with the observation that the smooth, thin Au can produce large-area exfoliation, while the rougher, thicker Au cannot. This reinforces our conclusion that the surface quality of Au is critical for the success of large-area exfoliation.

The most striking difference occurs in the electronic structure of  $\text{MoS}_2$ . The semiconducting character of free-standing  $\text{MoS}_2$  changes to metallic in the monolayer  $\text{MoS}_2$ /Au heterostructure (Fig. 5c). Indeed, the Bader charge analysis indicates a system-dependent electron transfer from Au to the monolayer  $\text{MoS}_2$  (Supporting Fig. S6). The resulting increase of the DOS at the Fermi level ( $E_F$ ) has a direct impact on the electrochemical behavior discussed below. These

states, which originate mainly from S 3s-*p* orbitals and Mo 4*d* orbitals, reside at the MoS<sub>2</sub>/Au interface (Fig. 5d–e).



**Figure 5 | vdW DFT calculations of the MoS<sub>2</sub>–Au interactions.** **a**, Binding energies determined for several different systems of monolayer MoS<sub>2</sub> on: pristine Au (111), Au (111) with a different number (*n*) of missing Au rows, and *m*–layer MoS<sub>2</sub>. **b**, Binding energy of monolayer MoS<sub>2</sub> on pristine Au as a function of the separation between Mo and Au atomic planes. The equilibrium separation was determined to be 4.5 Å, in good agreement with the experimental value from HAADF-STEM. **c**, DOS for free-standing monolayer MoS<sub>2</sub> (bottom panel), monolayer MoS<sub>2</sub> on pristine Au (middle panel), and monolayer MoS<sub>2</sub> on Au with 5 missing Au rows (top panel). **d–e**, Charge-density differences calculated for monolayer MoS<sub>2</sub> on: pristine Au (111) (**d**), 5 missing Au rows (**e**), plotted as  $\Delta\rho = \rho[\text{Au} + \text{MoS}_2] - \rho[\text{Au}] - \rho[\text{MoS}_2]$ , where the three latter terms are the total charge densities of monolayer MoS<sub>2</sub>/Au, Au slab, and monolayer MoS<sub>2</sub>, respectively.

## Electrochemical characterization of the MoS<sub>2</sub>–Au heterostructure

The large-area monolayer MoS<sub>2</sub> on Au is an excellent platform for investigations previously limited by the small lateral crystal size. Figure 6 shows the electrochemical characterization of three macroscopic ( $\sim 0.5$  mm<sup>2</sup>) surfaces: bare Au (gold), monolayer MoS<sub>2</sub>/Au (red), and bulk MoS<sub>2</sub> (gray). The kinetics of the reduction/oxidation of  $[\text{Ru}(\text{NH}_3)_6]^{3+/2+}$  and  $[\text{Fe}(\text{CN})_6]^{3-/4-}$  used as redox mediators, quantified by the heterogeneous electron transfer rate constant ( $k^0$ ), vary greatly on these surfaces, as illustrated by the voltammograms in Fig. 6a–b. Au exhibits the fastest, reversible kinetics for both mediators ( $k^0 > 1$  cm s<sup>-1</sup>), expected due to their fast self-exchange rates and the high DOS of Au. The  $k^0$  values on bulk MoS<sub>2</sub> are  $\sim 4 \times 10^{-4}$  cm s<sup>-1</sup> and  $< 10^{-7}$  cm s<sup>-1</sup> for  $[\text{Ru}(\text{NH}_3)_6]^{3+/2+}$  and  $[\text{Fe}(\text{CN})_6]^{3-/4-}$ , respectively, in agreement with previous work.<sup>32</sup> The kinetics of  $[\text{Ru}(\text{NH}_3)_6]^{3+/2+}$ , which is thought to be an outer-sphere mediator only sensitive to the surface DOS, are reversible on monolayer MoS<sub>2</sub>/Au and similar to that of bare Au (Fig. 6a), indicating strong electronic coupling and charge transfer between MoS<sub>2</sub> and Au, in agreement with our results above. The SECM imaging of the  $[\text{Ru}(\text{NH}_3)_6]^{3+/2+}$  redox activity of MoS<sub>2</sub> on Au (Fig. 6c–e) shows a clear correlation with the corresponding optical image (Fig. 6f). As the number of MoS<sub>2</sub> layers decreases, the normalized current ( $I / I_0$ ) increases, indicating a transition from the semiconducting multilayer MoS<sub>2</sub> to the metallic monolayer MoS<sub>2</sub>/Au in agreement with the predicted increase in DOS (Fig. 5f), with the highest current observed for the bare Au. In contrast, the kinetics of  $[\text{Fe}(\text{CN})_6]^{3-/4-}$  on monolayer MoS<sub>2</sub>/Au slows down by 6 orders of magnitude to  $\sim 1 \times 10^{-4}$  cm s<sup>-1</sup> within the quasi-reversible regime (Fig. 6b). The strong suppression of the kinetics of  $[\text{Fe}(\text{CN})_6]^{3-/4-}$ , which is an inner-sphere mediator interacting strongly with the electrode surface, indicates that the Au surface is strongly passivated by the MoS<sub>2</sub> monolayer. In addition, the open circuit potential in 1 M KCl was found to be the same for monolayer MoS<sub>2</sub>/Au and bulk MoS<sub>2</sub> (0.000 V), but considerably different for Au (0.034 V). No

dependence on illumination was observed for monolayer MoS<sub>2</sub>/Au, as expected. These results suggest that monolayer MoS<sub>2</sub>/Au is chemically similar to MoS<sub>2</sub> but has an increased DOS acquired from the underlying Au. In other words, monolayer MoS<sub>2</sub>/Au is thermodynamically closer to bulk MoS<sub>2</sub> but kinetically closer to Au. These characteristics could be effectively used to discriminate between the outer- and inner-sphere electron transfer mechanisms. A similar concept of electronic modulation was recently demonstrated for graphene on Au.<sup>33</sup>

Capacitance measurements in 1 M KCl also reveal significant differences between the three surfaces (Fig. 6g). The interfacial (measured) capacitance  $C_{\text{int}}$  is a sum of two capacitances in series:  $C_{\text{int}}^{-1} = C_{\text{SC}}^{-1} + C_{\text{EDL}}^{-1}$ , where  $C_{\text{SC}}$  and  $C_{\text{EDL}}$  are the space charge and electrical double-layer capacitances at the electrode/liquid interface<sup>34</sup>.  $C_{\text{int}} = 34 \mu\text{F cm}^{-2}$  for bare Au and is equal to  $C_{\text{EDL}}$  due to the efficient Thomas-Fermi screening in metals ( $C_{\text{SC}} \gg C_{\text{EDL}}$ ).  $C_{\text{int}} = 0.7 \mu\text{F cm}^{-2}$  in bulk MoS<sub>2</sub> and is equal to  $C_{\text{SC}}$ , since in semiconductors  $C_{\text{SC}} \ll C_{\text{EDL}}$ . An intermediate  $C_{\text{int}} = 3 \mu\text{F cm}^{-2}$  in monolayer MoS<sub>2</sub>/Au is mostly dominated by  $C_{\text{SC}}$  ( $C_{\text{int}} \approx 0.9C_{\text{SC}}$ , calculated using the  $C_{\text{EDL}}$  determined for Au). The shapes of the voltammograms in Fig. 6g reflect the differing electronic band structures of the three different surfaces. The metallic Au behaves as a typical pseudocapacitor with a redox (faradaic) activity superimposed over the double-layer charging at high potentials. The response of bulk MoS<sub>2</sub> is typical for an n-type semiconductor, with the higher currents at low potentials corresponding to the charge carrier accumulation regime. Surprisingly, monolayer MoS<sub>2</sub>/Au exhibits a rectangular-shaped voltammogram, indicating a purely capacitive (non-faradaic) response, which originates solely from the double-layer charging. Such potential-independent capacitance response, which is typical of an electrochemical supercapacitor,<sup>35-36</sup> is significantly different from the responses of bulk MoS<sub>2</sub> and bare Au. This suggests that monolayer MoS<sub>2</sub>/Au system (and potentially many other TMDCs/Au) could provide an interesting platform

for the design of supercapacitors and other devices for electrochemistry, photocatalysis and energy storage/conversion.

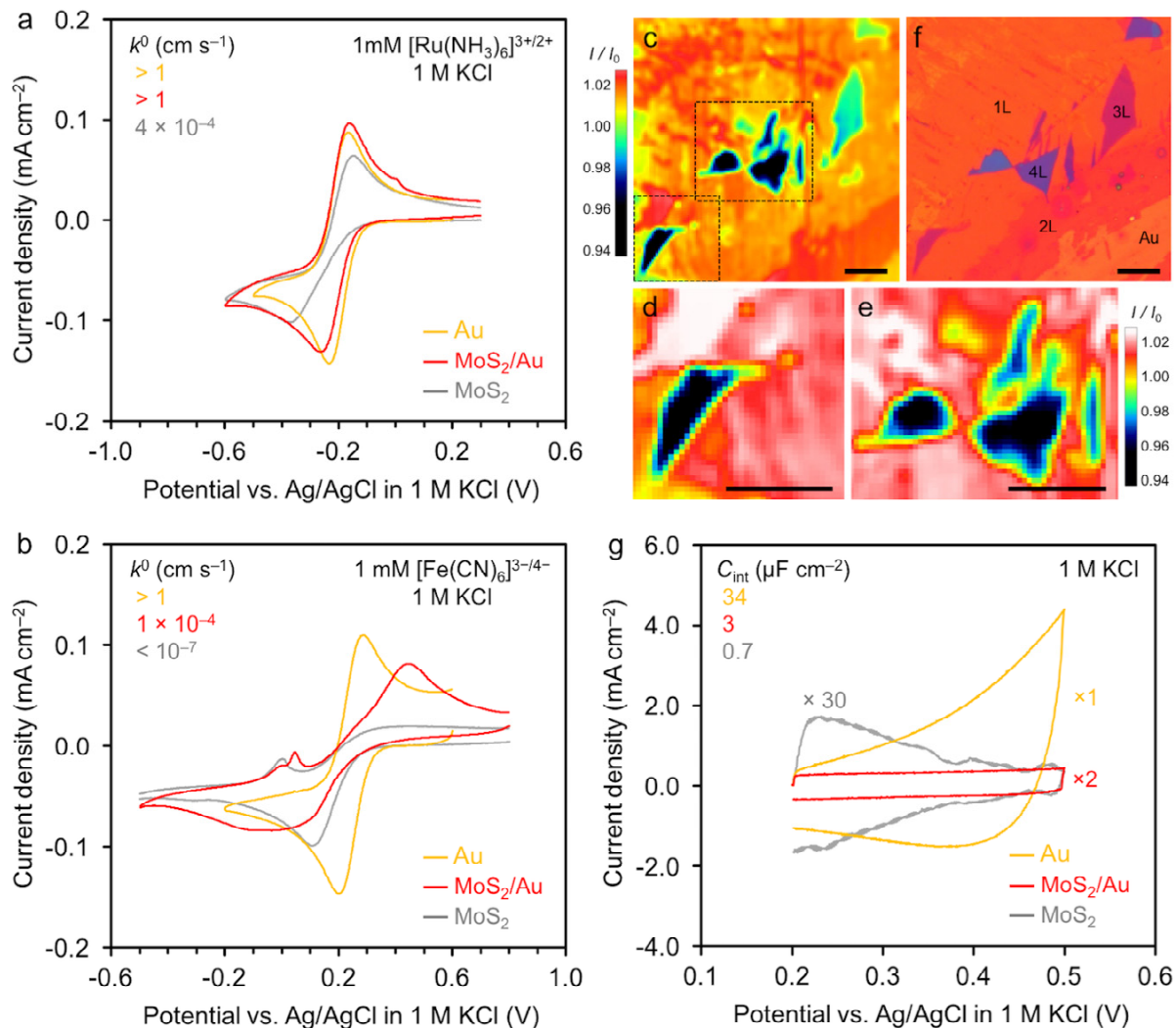


**Figure 6 | Electrochemical characterization of  $\text{MoS}_2$  on Au.** **a–b,** Cyclic voltammograms of  $1 \text{ mM } [\text{Ru}(\text{NH}_3)_6]^{3+/2+}$  and  $1 \text{ mM } [\text{Fe}(\text{CN})_6]^{3-/4-}$  reduction/oxidation in  $1 \text{ M KCl}$  at  $50 \text{ mV s}^{-1}$ , respectively. Results for the bare Au surface (gold), monolayer  $\text{MoS}_2/\text{Au}$  (red), and bulk  $\text{MoS}_2$  (gray), are shown. **c,** SECM image of different  $\text{MoS}_2$  layers on Au, generated in feedback mode using  $1 \text{ mM } [\text{Ru}(\text{NH}_3)_6]^{3+/2+}$  in  $0.1 \text{ M KCl}$ . **d–e,** Magnified SECM images taken from regions highlighted in **c** by the black rectangles. **f,** Corresponding optical image of the measured area. All scale bars correspond to  $40 \mu\text{m}$ . **g,** Cyclic voltammograms in  $1 \text{ M KCl}$  at  $50 \text{ V s}^{-1}$  for the determination of the interfacial capacitance. All measurements were carried out under ambient light at room temperature and argon-deaerated solutions were used in **a–b** and **g**.

## CONCLUSIONS

We present a facile gold-assisted mechanical exfoliation of extraordinarily large monolayer MoS<sub>2</sub>, up to a centimeter-scale, limited mainly by the parent bulk crystal size. We carried out detailed spectroscopic and microscopic characterizations together with first-principles DFT calculations to provide an atomic-level understanding of the exfoliation mechanism. The large-area exfoliation is found to be facilitated by strong vdW interaction between Au and the topmost layer of MoS<sub>2</sub>, which critically depends on the cleanliness and smoothness of the Au surface. Near-unity yield of monolayer MoS<sub>2</sub> is achieved on freshly-grown thin Au films (5–20 nm) with RMS roughness <1 nm and exposure to air for less than 6 min. The yield becomes negligible after 15 min of exposure due to the accumulation of airborne contamination on Au. Such previously unknown stringent experimental conditions have important consequences for the development of large-area exfoliation and growth techniques. We have successfully extended the technique to MoSe<sub>2</sub>, WS<sub>2</sub>, WSe<sub>2</sub>, MoTe<sub>2</sub>, WTe<sub>2</sub> and GaSe. Electrochemical characterization reveals that the surface DOS of monolayer MoS<sub>2</sub> is strongly modulated by the underlying Au, turning it from semiconducting to metallic. Conversely, the sub-nanometer thick monolayer MoS<sub>2</sub> strongly passivates the chemistry of the underlying Au electrode, but does not prevent charge transfer from solution to Au. Our work sheds light on the mechanism of gold-assisted exfoliation, provides important guidance for the production of macroscopic TMDC monolayers, and has important implications for many research areas, such as electrode modification, photovoltaics, and photocatalysis.

## METHODS

### Materials preparation

PVD films were prepared with a DC magnetron sputtering system (Kurt J. Lesker CMS-A) using targets (> 99.99%) from Testbourne Ltd (Ti) and Birmingham Metal Ltd (Au). The SiO<sub>2</sub>/Si wafers (IDB Technologies Ltd) were cleaned in acetone, isopropanol, and blow-dried before placing in a load-lock, evacuated to  $\sim 10^{-7}$  Torr by a turbomolecular pump (Shimadzu TMP-303LM) backed by a mechanical pump (Adixen ACP 15). They were then transferred to the deposition chamber, evacuated to  $\sim 10^{-9}$  Torr using a cryopump (Brooks CTI-Cryogenics 10F). All the pumps were oil-free and the residual gas environment was continuously monitored by mass spectrometry prior to the sputtering. Depositions were done at room temperature under a 5 SCCM Ar flow at partial pressure of 10<sup>-3</sup> Torr. A Ti adhesion layer was deposited at 15° incidence at a rate of 0.5 Å s<sup>-1</sup> before the main metal deposition. The Au layer was deposited at a 33° incidence at a rate of 1.5 Å s<sup>-1</sup>. All targets were pre-sputtered prior to the deposition. All metal chalcogenides were exfoliated from bulk crystals (Manchester Nanomaterials Ltd) directly onto the Au substrates using the “scotch-tape” method reported elsewhere,<sup>37</sup> applying a downward pressure, rather than lateral rubbing. The crystals were exfoliated, and therefore exposed to air, immediately prior to the contact with Au (<5 s) in order to minimize the airborne contamination of their surface. Bulk crystals were either natural (molybdenite) or synthesized by chemical vapor transport (MoSe<sub>2</sub>, MoTe<sub>2</sub>, WS<sub>2</sub>, WSe<sub>2</sub>, WTe<sub>2</sub>, and GaSe). The exfoliation and subsequent characterization (except the vacuum techniques) were performed at 20–23 °C and 50–70% relative humidity.

### Microscopy, spectroscopy, reflectivity, and diffraction characterization

Macroscopic optical images were taken using a Canon PowerShot A720 IS digital camera. Microscopic optical images were taken using a BX51 microscope (Olympus Corp) with an

Infinity2-2 CCD camera and Infinity Capture 6.2 software (Lumenera Corp). The exfoliation yield should ideally be calculated as the ratio between the areas of the exfoliated and parent MoS<sub>2</sub> crystals. However, as the size of the parent crystals and their surface defect and impurity densities vary for different exfoliations, such approach is impractical. To circumvent this uncertainty, we used a constant sampling area (rather than the actual parent crystal size) for each yield comparison, chosen as large as possible to approximate the largest continuous area of the exfoliated MoS<sub>2</sub>. Specifically, identical squares of  $0.5 \times 0.5 \text{ cm}^2$  and  $110 \times 110 \text{ } \mu\text{m}^2$  at three different locations on the wafer were used as sampling areas for the ageing- and roughness-dependent yield determination, respectively, allowing meaningful quantitative comparison of the yield dependence on the surface condition of Au. The exfoliation yield ( $Y$ ) was then calculated as  $Y(\%) = A_M / A_S \times 100\%$ , where  $A_M$  is the area covered by MoS<sub>2</sub> and  $A_S$  is the sampled area, both of which were determined from the optical image using Fiji/ImageJ software (v.2.0). 532 nm or 633 nm lasers of 1 mW power focused through a 100 $\times$  MPlan N objective (Olympus Corp) to  $\sim 1 \text{ } \mu\text{m}^2$  spot size were used for Raman spectroscopy and PL measurements, collected by a Jobin Yvon HR640 Raman spectrometer and Andor MCD 2.6 software. AFM measurements were performed with a Digital Instruments Veeco Dimension 300 AFM with 30 nm Si-SPM tips (Nanosensors™) in tapping mode. The contact angle measurements were carried out using a Dino-Lite Edge AM7115MZTL Digital microscope and in-house rotating-state goniometer. A field emission JEOL JSM-6500F SEM at an accelerating voltage of 5–10 kV was used for SEM imaging. The X-ray reflectivity and XRD, taken using a D8 Discover diffractometer (Bruker Inc), were used to determine the thickness and crystallographic orientation of Au, respectively. XPS was performed using a non-monochromatic Mg K $\alpha$  source, collecting the photoelectrons at glancing incidence from the surface normal, from an area of  $\sim 0.8 \text{ cm}^2$ . The spectrometer energy analyzer work function was calibrated using an Ag standard. Tougaard baseline subtraction and normalization to

the maximum intensity were applied to all spectra. STEM samples were prepared in a FEI Strata 400 focused ion beam using a standard cross-section fabrication procedure.<sup>38</sup> STEM and EELS imaging were performed using a NION UltraSTEM operated at 100 keV.

## Computational methods

First principles *ab initio* calculations were carried out with the Vienna *ab initio* simulation package.<sup>39</sup> The generalized gradient approximation<sup>40</sup> along with the Tkatchenko-Scheffler method<sup>41</sup> were used to correct the energy due to dispersion interactions. This was used along with a 345 eV plane-wave cut-off. The projector augmented wave pseudopotentials<sup>42-43</sup> were utilized to model the bonding environment between atoms. Energy convergence for the electronic and ionic minimizations was set at  $1 \times 10^{-5}$  and  $1 \times 10^{-4}$  eV, respectively. Au (111) and monolayer MoS<sub>2</sub> unit cells were relaxed with a  $12 \times 12 \times 6$  and  $12 \times 12 \times 1$   $\Gamma$ -centered k-grid respectively. From this an  $8 \times 8 \times 4$  Au surface was created as well as a  $7 \times 7 \times 1$  MoS<sub>2</sub> supercell. This resulted in  $\sim 1.0\%$  lattice mismatch, which was applied to the Au surface to avoid spurious variation on the strain sensitive MoS<sub>2</sub> energetics. The bottom two Au layers were fixed as bulk while the top two Au layers, representing the surface, were allowed to relax. After the introduction of defects, the Au surface was allowed to relax further. The MoS<sub>2</sub> supercell was then placed on top of the Au surface and the MoS<sub>2</sub>/Au heterostructure was allowed to relax once again. Binding energies of 1L MoS<sub>2</sub> on  $m-$ layer MoS<sub>2</sub> were calculated as  $E_B = E_{(m+1)L} - E_{mL} - E_{1L}$ , where  $E_{(m+1)L}$ ,  $E_{mL}$ , and  $E_{1L}$  are the total energies of  $(m+1)-$ ,  $m-$ , and 1-layer MoS<sub>2</sub>, respectively. Binding energies of 1L MoS<sub>2</sub> on Au systems were calculated as  $E_B = E_{1L+Au} - E_{Au} - E_{1L}$ , where  $E_{1L+Au}$  and  $E_{Au}$  are the total energies of 1L MoS<sub>2</sub> on Au and the Au slab, respectively.

## Electrochemical measurements

All electrochemical measurements were performed using a CHI920D potentiostat (CH Instruments, Inc.). The electrochemical setup is schematically shown in Supporting Fig. S7. The  $k^0$  values were estimated from the peak-to-peak separation in the voltammograms (10–400 mV s<sup>-1</sup>). This was done using the Nicholson method and the Klingler-Kochi method in the reversible-quasireversible and irreversible regime, respectively, following the methodology reported elsewhere (Eq. (1) and Eq. (2) in ref<sup>44</sup>, respectively). Diffusion coefficients of  $7.4 (5.3) \times 10^{-6}$  cm<sup>2</sup> s<sup>-1</sup> and  $7.7 (6.2) \times 10^{-6}$  cm<sup>2</sup> s<sup>-1</sup> for the oxidized (reduced) forms of  $[\text{Ru}(\text{NH}_3)_6]^{3+/2+}$  and  $[\text{Fe}(\text{CN})_6]^{3-4-}$ , respectively, were determined from voltammetry at polished 2 mm diameter Pt disk using the Randles-Ševčík equation.<sup>35</sup> The interfacial capacitance ( $C_{\text{int}}$ ) was calculated by integrating the current over the potential range as described elsewhere<sup>45</sup> and averaged for scan rates between 10–50 V s<sup>-1</sup>. The reference potential used here (Ag/AgCl in 1 M KCl) is +0.232 V on the standard hydrogen electrode scale, taking the activity coefficient of Cl<sup>-</sup> into account.<sup>46</sup> SECM was obtained using a 1  $\mu\text{m}$  diameter Pt ultramicroelectrode probe with a glass radius of  $\sim 25 \mu\text{m}$  (Heka), operated in the feedback mode at a working distance of ca. 1  $\mu\text{m}$ . The probe potential was set to reduce/oxidize  $[\text{Ru}(\text{NH}_3)_6]^{3+/2+}$  under diffusion control while the substrate was unbiased. The probe current ( $I$ ) measured near the surface was normalized to the current in bulk solution ( $I_0$ ).

## ASSOCIATED CONTENT

**Supporting Information.** Optical micrographs of various metal chalcogenide monolayers exfoliated on Au substrate; PL measurement of MoS<sub>2</sub> on Au, water contact angle measurement on Au as a function of its exposure to air; XRD measurement of the Au films; detailed XPS spectra including peak fittings; Bader charge transfer analysis of MoS<sub>2</sub>/Au heterostructures.

## AUTHOR INFORMATION

### Corresponding Authors.

\*Email: [f.huang@qub.ac.uk](mailto:f.huang@qub.ac.uk) and [mv337@cornell.edu](mailto:mv337@cornell.edu).

### ORCID

Matěj Velický: 0000-0003-4230-3811

Andrew J. Wain: 0000-0002-8666-6158

Robert M. Bowman: 0000-0002-4855-2387

Fumin Huang: 0000-0001-6489-9818

### Notes

The authors declare no competing financial interest.

## ACKNOWLEDGEMENTS

This project has received funding from the UK EPSRC (grant No. EP/N025938/1), the European Union's Horizon 2020 research and innovation programme under the Marie Skłodowska-Curie grant agreement No. 746685, and the UK National Measurement System (Department of Business, Energy & Industrial Strategy), and was supported by Seagate Technology (Ireland) under SOW #00077300.0 & the Royal Academy of Engineering under the Research Chairs and Senior Research Fellowships Scheme, CCMR (NSF-DMR-1719875), PARADIM (NSF-DMR-1539918), DOE CSGF (DE-FG02-97ER25308), NSF-CHE-1708025, and the Alfred P. Sloan Foundation. E.J.G.S. acknowledges the use of computational resources from the UK national high-performance computing service (ARCHER) for which access was obtained *via* the UKCP consortium (EPSRC grant ref EP/K013564/1), the UK Materials and Molecular Modelling Hub for access to THOMAS supercluster, which is partially funded by EPSRC (EP/P020194/1). The Queen's Fellow Award

(M8407MPH), the Enabling Fund (A5047TSL), and the Department for the Economy (USI 097) are also acknowledged.

## REFERENCES

(1) Peña-Álvarez, M.; del Corro, E.; Morales-García, Á.; Kavan, L.; Kalbac, M.; Frank, O., Single Layer Molybdenum Disulfide under Direct Out-of-Plane Compression: Low-Stress Band-Gap Engineering. *Nano Lett.* 2015, 15 (5), 3139-3146.

(2) Mak, K. F.; Lee, C.; Hone, J.; Shan, J.; Heinz, T. F., Atomically Thin MoS<sub>2</sub>: A New Direct-Gap Semiconductor. *Phys. Rev. Lett.* 2010, 105 (13), 136805.

(3) Velicky, M.; Toth, P. S., From Two-Dimensional Materials to Their Heterostructures: An Electrochemist's Perspective. *Appl. Mater. Today* 2017, 8, 68-103.

(4) Withers, F.; Del Pozo-Zamudio, O.; Mishchenko, A.; Rooney, A. P.; Gholinia, A.; Watanabe, K.; Taniguchi, T.; Haigh, S. J.; Geim, A. K.; Tartakovskii, A. I.; Novoselov, K. S., Light-Emitting Diodes by Band-Structure Engineering in van der Waals Heterostructures. *Nat. Mater.* 2015, 14 (3), 301-306.

(5) Lee, H. S.; Min, S.-W.; Chang, Y.-G.; Park, M. K.; Nam, T.; Kim, H.; Kim, J. H.; Ryu, S.; Im, S., MoS<sub>2</sub> Nanosheet Phototransistors with Thickness-Modulated Optical Energy Gap. *Nano Lett.* 2012, 12 (7), 3695-3700.

(6) Bernardi, M.; Palummo, M.; Grossman, J. C., Extraordinary Sunlight Absorption and One Nanometer Thick Photovoltaics Using Two-Dimensional Monolayer Materials. *Nano Lett.* 2013, 13 (8), 3664-3670.

(7) Coleman, J. N.; Lotya, M.; O'Neill, A.; Bergin, S. D.; King, P. J.; Khan, U.; Young, K.; Gaucher, A.; De, S.; Smith, R. J.; Shvets, I. V.; Arora, S. K.; Stanton, G.; Kim, H. Y.; Lee, K.; Kim, G. T.; Duesberg, G. S.; Hallam, T.; Boland, J. J.; Wang, J. J.; et al., Two-Dimensional Nanosheets Produced by Liquid Exfoliation of Layered Materials. *Science* 2011, 331 (6017), 568-571.

(8) Wang, X.; Gong, Y.; Shi, G.; Chow, W. L.; Keyshar, K.; Ye, G.; Vajtai, R.; Lou, J.; Liu, Z.; Ringe, E.; Tay, B. K.; Ajayan, P. M., Chemical Vapor Deposition Growth of Crystalline Monolayer MoSe<sub>2</sub>. *ACS Nano* 2014, 8 (5), 5125-5131.

(9) Novoselov, K. S.; Jiang, D.; Schedin, F.; Booth, T. J.; Khotkevich, V. V.; Morozov, S. V.; Geim, A. K., Two-Dimensional Atomic Crystals. *Proc. Natl. Acad. Sci. U. S. A.* 2005, 102 (30), 10451-10453.

(10) Velicky, M.; Bissett, M. A.; Woods, C. R.; Toth, P. S.; Georgiou, T.; Kinloch, I. A.; Novoselov, K. S.; Dryfe, R. A. W., Photoelectrochemistry of Pristine Mono- and Few-Layer MoS<sub>2</sub>. *Nano Lett.* 2016, 16 (3), 2023-2032.

(11) Desai, S. B.; Madhvapathy, S. R.; Amani, M.; Kiriya, D.; Hettick, M.; Tosun, M.; Zhou, Y.; Dubey, M.; Ager, J. W.; Chrzan, D.; Javey, A., Gold-Mediated Exfoliation of Ultralarge Optoelectronically-Perfect Monolayers. *Adv. Mater.* 2016, 28 (21), 4053-4058.

(12) Magda, G. Z.; Pető, J.; Dobrik, G.; Hwang, C.; Biró, L. P.; Tapasztó, L., Exfoliation of Large-Area Transition Metal Chalcogenide Single Layers. *Sci. Rep.* 2015, 5, 14714.

(13) Lee, C.; Yan, H.; Brus, L. E.; Heinz, T. F.; Hone, J.; Ryu, S., Anomalous Lattice Vibrations of Single- and Few-Layer MoS<sub>2</sub>. *ACS Nano* 2010, 4 (5), 2695-2700.

(14) Li, H.; Zhang, Q.; Yap, C. C. R.; Tay, B. K.; Edwin, T. H. T.; Olivier, A.; Baillargeat, D., From Bulk to Monolayer MoS<sub>2</sub>: Evolution of Raman Scattering. *Adv. Funct. Mater.* 2012, 22 (7), 1385-1390.

(15) Robinson, B. J.; Giusca, C. E.; Gonzalez, Y. T.; Kay, N. D.; Kazakova, O.; Kolosov, O. V., Structural, Optical and Electrostatic Properties of Single and Few-Layers MoS<sub>2</sub>: Effect of Substrate. *2D Mater.* 2015, 2 (1), 015005.

(16) Bhanu, U.; Islam, M. R.; Tetard, L.; Khondaker, S. I., Photoluminescence Quenching in Gold - MoS<sub>2</sub> Hybrid Nanoflakes. *Sci. Rep.* 2014, 4, 5575.

(17) Buscema, M.; Steele, G. A.; van der Zant, H. S. J.; Castellanos-Gomez, A., The Effect of the Substrate on the Raman and Photoluminescence Emission of Single-Layer MoS<sub>2</sub>. *Nano Res.* 2014, 7 (4), 1-11.

(18) Najmaei, S.; Mlayah, A.; Arbouet, A.; Girard, C.; Léotin, J.; Lou, J., Plasmonic Pumping of Excitonic Photoluminescence in Hybrid MoS<sub>2</sub>–Au Nanostructures. *ACS Nano* 2014, 8 (12), 12682-12689.

(19) Smith, T., The Hydrophilic Nature of a Clean Gold Surface. *J. Colloid Interface Sci.* 1980, 75 (1), 51-55.

(20) Todeschini, M.; Bastos da Silva Fanta, A.; Jensen, F.; Wagner, J. B.; Han, A., Influence of Ti and Cr Adhesion Layers on Ultrathin Au Films. *ACS Appl. Mater. Interfaces* 2017, 9 (42), 37374-37385.

(21) Adamov, M.; Perović, B.; Nenadović, T., Electrical and Structural Properties of Thin Gold Films Obtained by Vacuum Evaporation and Sputtering. *Thin Solid Films* 1974, 24 (1), 89-100.

(22) Parajuli, P.; Mendoza-Cruz, R.; Santiago, U.; Ponce, A.; Yacamán, M. J., The Evolution of Growth, Crystal Orientation, and Grain Boundaries Disorientation Distribution in Gold Thin Films. *Cryst. Res. Technol.* 2018, 53 (8), 1800038.

(23) Skriver, H. L.; Rosengaard, N. M., Surface Energy and Work Function of Elemental Metals. *Phys. Rev. B* 1992, 46 (11), 7157-7168.

(24) Zhong, H.; Quhe, R.; Wang, Y.; Ni, Z.; Ye, M.; Song, Z.; Pan, Y.; Yang, J.; Yang, L.; Lei, M.; Shi, J.; Lu, J., Interfacial Properties of Monolayer and Bilayer MoS<sub>2</sub> Contacts with Metals: Beyond the Energy Band Calculations. *Sci. Rep.* 2016, 6, 21786.

(25) Farmanbar, M.; Brocks, G., First-Principles Study of van der Waals Interactions and Lattice Mismatch at MoS<sub>2</sub>/Metal Interfaces. *Phys. Rev. B* 2016, 93 (8), 085304.

(26) Kokkin, D. L.; Zhang, R.; Steimle, T. C.; Wyse, I. A.; Pearlman, B. W.; Varberg, T. D., Au–S Bonding Revealed from the Characterization of Diatomic Gold Sulfide, AuS. *J. Phys. Chem. A* 2015, 119 (48), 11659-11667.

(27) Lince, J. R.; Carré, D. J.; Fleischauer, P. D., Schottky-Barrier Formation on a Covalent Semiconductor Without Fermi-Level Pinning: The Metal-MoS<sub>2</sub>(0001) Interface. *Phys. Rev. B* 1987, 36 (3), 1647-1656.

(28) Bruix, A.; Füchtbauer, H. G.; Tuxen, A. K.; Walton, A. S.; Andersen, M.; Porsgaard, S.; Besenbacher, F.; Hammer, B.; Lauritsen, J. V., *In Situ* Detection of Active Edge Sites in Single-Layer MoS<sub>2</sub> Catalysts. *ACS Nano* 2015, 9 (9), 9322-9330.

(29) Shi, J.; Yang, Y.; Zhang, Y.; Ma, D.; Wei, W.; Ji, Q.; Zhang, Y.; Song, X.; Gao, T.; Li, C.; Bao, X.; Liu, Z.; Fu, Q.; Zhang, Y., Monolayer MoS<sub>2</sub> Growth on Au Foils and On-Site Domain Boundary Imaging. *Adv. Funct. Mater.* 2015, 25 (6), 842-849.

(30) Jette, E. R.; Foote, F., Precision Determination of Lattice Constants. *J. Chem. Phys.* 1935, 3 (10), 605-616.

(31) Björkman, T.; Gulans, A.; Krasheninnikov, A. V.; Nieminen, R. M., van der Waals Bonding in Layered Compounds from Advanced Density-Functional First-Principles Calculations. *Phys. Rev. Lett.* 2012, 108 (23), 235502.

(32) Velický, M.; Bissett, M. A.; Toth, P. S.; Patten, H. V.; Worrall, S. D.; Rodgers, A. N. J.; Hill, E. W.; Kinloch, I. A.; Novoselov, K. S.; Georgiou, T.; Britnell, L.; Dryfe, R. A. W., Electron Transfer Kinetics on Natural Crystals of MoS<sub>2</sub> and Graphite. *Phys. Chem. Chem. Phys.* 2015, 17 (27), 17844-17853.

(33) Hui, J.; Zhou, X.; Bhargava, R.; Chinderle, A.; Zhang, J.; Rodríguez-López, J., Kinetic Modulation of Outer-Sphere Electron Transfer Reactions on Graphene Electrode with a Sub-surface Metal Substrate. *Electrochim. Acta* 2016, 211, 1016-1023.

(34) Bott, A. W., Electrochemistry of Semiconductors. *Curr. Sep.* 1998, 17, 87-92.

(35) Bard, A. J.; Faulkner, L. R., *Electrochemical Methods. Fundamentals and Applications*. 2nd ed.; John Wiley & Sons, Inc.: New York, 2001.

(36) Conway, B. E., *Electrochemical Supercapacitors. Scientific Fundamentals and Technological Applications*. 1st ed.; Springer US: 1999; p 698.

(37) Novoselov, K. S.; Castro Neto, A. H., Two-Dimensional Crystals-Based Heterostructures: Materials with Tailored Properties. *Phys. Scr.* 2012, 2012 (T146), 014006.

(38) Giannuzzi, L. A.; Stevie, F. A., *Introduction to Focused Ion Beams: Instrumentation, Theory, Techniques and Practice*. Springer, Boston, MA: 2005.

(39) Kresse, G.; Hafner, J., *Ab initio* Molecular Dynamics for Open-Shell Transition Metals. *Phys. Rev. B* 1993, 48 (17), 13115-13118.

(40) Perdew, J. P.; Burke, K.; Ernzerhof, M., Generalized Gradient Approximation Made Simple. *Phys. Rev. Lett.* 1996, 77 (18), 3865-3868.

(41) Tkatchenko, A.; Scheffler, M., Accurate Molecular Van Der Waals Interactions from Ground-State Electron Density and Free-Atom Reference Data. *Phys. Rev. Lett.* 2009, 102 (7), 073005.

(42) Blöchl, P. E., Projector Augmented-Wave Method. *Phys. Rev. B* 1994, 50 (24), 17953-17979.

(43) Kresse, G.; Joubert, D., From Ultrasoft Pseudopotentials to the Projector Augmented-Wave Method. *Phys. Rev. B* 1999, 59 (3), 1758-1775.

(44) Velický, M.; Toth, P. S.; Rakowski, A. M.; Rooney, A. P.; Kozikov, A.; Woods, C. R.; Mishchenko, A.; Fumagalli, L.; Yin, J.; Zólyomi, V.; Georgiou, T.; Haigh, S. J.; Novoselov, K. S.; Dryfe, R. A. W., Exfoliation of Natural van der Waals Heterostructures to a Single Unit Cell Thickness. *Nat. Commun.* 2017, 8, 14410.

(45) Xiong, G.; Meng, C.; Reifenberger, R. G.; Irazoqui, P. P.; Fisher, T. S., A Review of Graphene-Based Electrochemical Microsupercapacitors. *Electroanalysis* 2014, 26 (1), 30-51.

(46) Khoshkbarchi, M. K.; Vera, J. H., Measurement and Correlation of Ion Activity in Aqueous Single Electrolyte Solutions. *AIChE J.* 1996, 42 (1), 249-258.